— 8 —

The Radiometric Calibration of the Extreme Ultraviolet Imaging Telescope

FRÉDÉRIC CLETTE, JEAN-FRANÇOIS HOCHEDEZ
Observatoire Royal de Belgique
Bruxelles, Belgium

JEFFREY S. NEWMARK, J. DANIEL MOSES
Naval Research Laboratory
Washington, DC, USA

FRÉDÉRIC AUCHÈRE
Universities Space Research Association/NASA GSFC
Greenbelt, MD, USA

JEAN-MARC DEFISE
Centre Spatial de Liège
Angleur-Liège, Belgium

JEAN-PIERRE DELABOUDINIÈRE
Institut d'Astrophysique Spatiale
Orsay, France

After a five-year effort, the analysis of the pre-flight and in-flight calibrations of EIT is finally yielding firm results. In this introductory overview, we will summarize what we learned "internally" from EIT itself. This includes the interpretation of the pre-flight calibrations, the original flat-field components (CCD, grid), the in-flight determination of the point-spread function and straylight and the compensation of the in-orbit response degradation. Based on this experience, we conclude with some suggestions of possible improvements to future calibrations, on SOHO and other planned missions.

8.1 Instrument Description

EIT, the Extreme ultraviolet Imaging Telescope experiment was designed to provide whole-disk images of the lower corona in four extreme-ultraviolet (EUV) bandpasses [*Delaboudinière et al.*, 1995; *Moses et al.*, 1997]. It consists of a normal-incidence Ritchey-Chrétien telescope using multilayer optics, with a back-side illuminated, thinned CCD sensor at the primary focus.

As illustrated in Figure 8.1, the components contributing to the EIT response are the visible-light rejection filters (transmittances of entrance-aperture filters, filter-wheel and straylight filters), the mirrors (reflectances and bandpasses), the CCD sensor (quantum efficiency), as well as some vignetting due to internal light-baffles. A large effort has been put forth into understanding the spectral response, the absolute calibration and the instrument

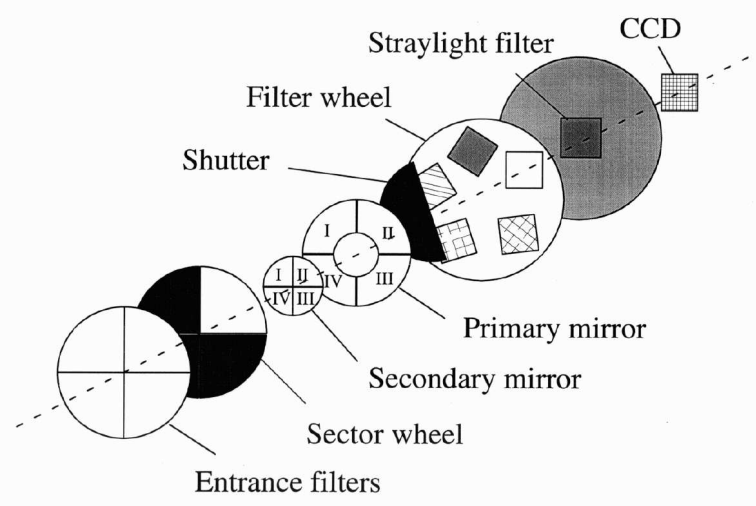

Figure 8.1: Optical components of EIT.

responsivity changes. This happened in two mains steps: the pre-launch laboratory characterization of a limited set of instrument properties and a comprehensive time-dependent radiometric calibration. This calibration was only achieved recently, several years into the SOHO mission, in part because this required data accumulation over a long time interval.

As EIT was among the very first EUV instruments based on normal-incidence multilayer optics, its initial calibration requirements were conservative ($\approx$ 100 %). However, the in-flight experience showed that much better accuracies were achievable and also essential for many scientific applications which emerged in the course of the SOHO mission. For instance, long-term solar cycle studies, made possible by SOHO's extended lifetime, require the compensation of slow instrumental trends. At the other extreme, short-term solar dynamics studies suffer from uncorrected sensor non-uniformities, as the solar rotation translates such spatial variations into fast random or periodic modulations. Therefore, the improved EIT calibration opens new fields of investigation, which were not considered among EIT's prime goals, but for which this EUV imager proved to be a unique source of information.

8.2 Pre-flight Calibration

The pre-launch calibration allowed the determination of component efficiencies (filters, mirrors, CCD) and the global instrumental efficiency as a function of wavelength: the absolute spectral response over the four EIT bandpasses. It also led to the determination of the initial CCD flat-field.

8.2.1 Spectral Response

The calibration measurements were carried out at the Institut d'Astrophysique Spatiale (IAS), in Orsay, France in 1993 to 1994 using synchrotron radiation from the Super-ACO

Table 8.1: Chronological table of instrumental configurations used for the EIT calibration. In Nov. 1993 and Sept. 1994, EIT was tested with its flight mirrors and filters and two different CCD cameras. The flight camera configuration uses the FM1 head with CCD3 and was thoroughly characterized in Dec. 1994. No end-to-end calibration of EIT could be done with the flight camera.

Date	Camera head	CCD sensor	Setup
Nov. 1993	FM1	CCD1 “Techno”	EIT telescope
July 1994	FM1	CCD1 “Techno”	camera only
July 1994	FM2	CCD2 “Flight”	camera only
Sept. 1994	FM2	CCD2 “Flight”	EIT telescope
Dec. 1994	FM1	CCD3 “Realflight”	camera only

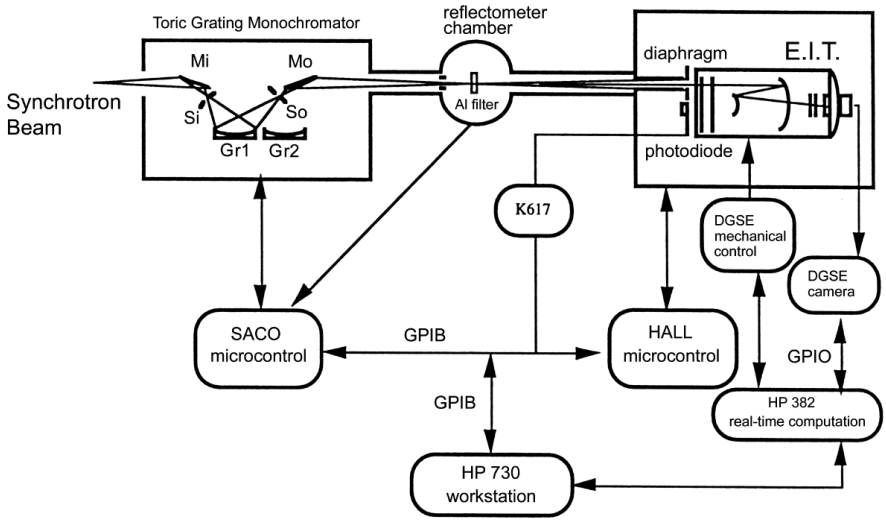

Figure 8.2: EIT calibration system at IAS.

positron storage ring [*Dhez et al.*, 1997]. A toroidal-grating monochromator allowed us to scan the whole EUV wavelength range observed by EIT. The standard of reference for all measurements was an IRD#925 Si photodiode calibrated by the National Institute of Standards and Technology (NIST, October 1993). This photodiode was placed in the incoming beam just in front of the EIT entrance pupil and alternately replaced by a square aperture of the same size. Three different CCD chips and two different camera heads were used in different configurations, which are summarized in Table 8.1. The calibration setup (Figure 8.2) and procedure are described in detail by *Song* [1995].

The analysis of these laboratory data has now been largely completed [*Dere et al.*, 2000; *Newmark et al.*, 2000a, b] and the results have been integrated in the EIT tools of the SolarSoftWare (SSW) library: for example `eit_prep`, `eit_parms`, `eit_flux`, `eit_temp`. Figure 8.3 shows the resulting EIT spectral response over the four EIT bandpasses.

The uncertainty budget published by Dere (Table V in *Dere et al.* [2000]) shows fairly high uncertainties, from 60 % to 150 % depending on the mirror quadrant, but is based on the discrepancies between a small number of spectral scans (geometrical averages). These conservative values can be considered as worst-case estimates and have subsequently been lowered, based on the in-flight calibrations (for example, see *Auchère* [2000]: 15 % instead of 75 % uncertainty at 30.4 nm).

8.2.2 CCD Flat-field Determination

Given the non-uniformity of the entrance synchrotron radiation beam, sequences of spatially displaced images were produced and each image set was processed using the Kuhn, Lin and Loranz algorithm (KLL; *Kuhn et al.* [1991]) to extract detector blemishes. Good flat-fields were obtained at two wavelengths: 17.1 nm and 28.4 nm (Figure 8.4, left). Those relative-correction maps were normalized to unity and have a relative standard uncertainty of 4 % (variable across the field-of-view). This correction is part of the SSW `eit_prep` tool. However, once in space, the CCD flat-field has been substantially modified, in particular in the strongest blemishes corresponding to sensor surface defects. The actual uncertainties are thus larger. Although no direct proof could be derived so far, this initial flat-field change may have been caused by chemical interactions with surface contaminants. Indeed, the existence of a thin water-ice deposit, which formed soon after launch, was firmly established through the initial changes in the EUV instrument responsivity and the presence of ice crystal patterns in the first EUV flat-fields, before the first detector bakeout of May 1996, which eliminated this ice.

8.3 In-flight Calibration: Flat-field and Other Diagnostics

Several components of the calibration could not be measured accurately on the ground and were extracted indirectly after launch from the solar images themselves.

8.3.1 Focal-filter Grid Correction

Several aluminium filters are located just in front of the focal plane: the fixed CCD straylight filter and the redundant filters on the filter wheel. To improve their mechanical strength, those filters are supported by a tungsten grid which casts an unsharp shadow-pattern on the CCD sensor (diffraction effects are negligible). This pattern is purely periodic (P = $\pm$21 pixels) and uniform over the field-of-view, but with a slight tilt angle relative to the edges of the CCD. It was extracted from smoothed solar images (8-day rotational averaging), by a Fourier transform and digital filtering (more than 40 harmonics).

An accurate correction pattern was derived out to the corners in the four quadrants and in the two main filter-wheel positions: Clear aperture and Al+1 redundant filter (Fig-

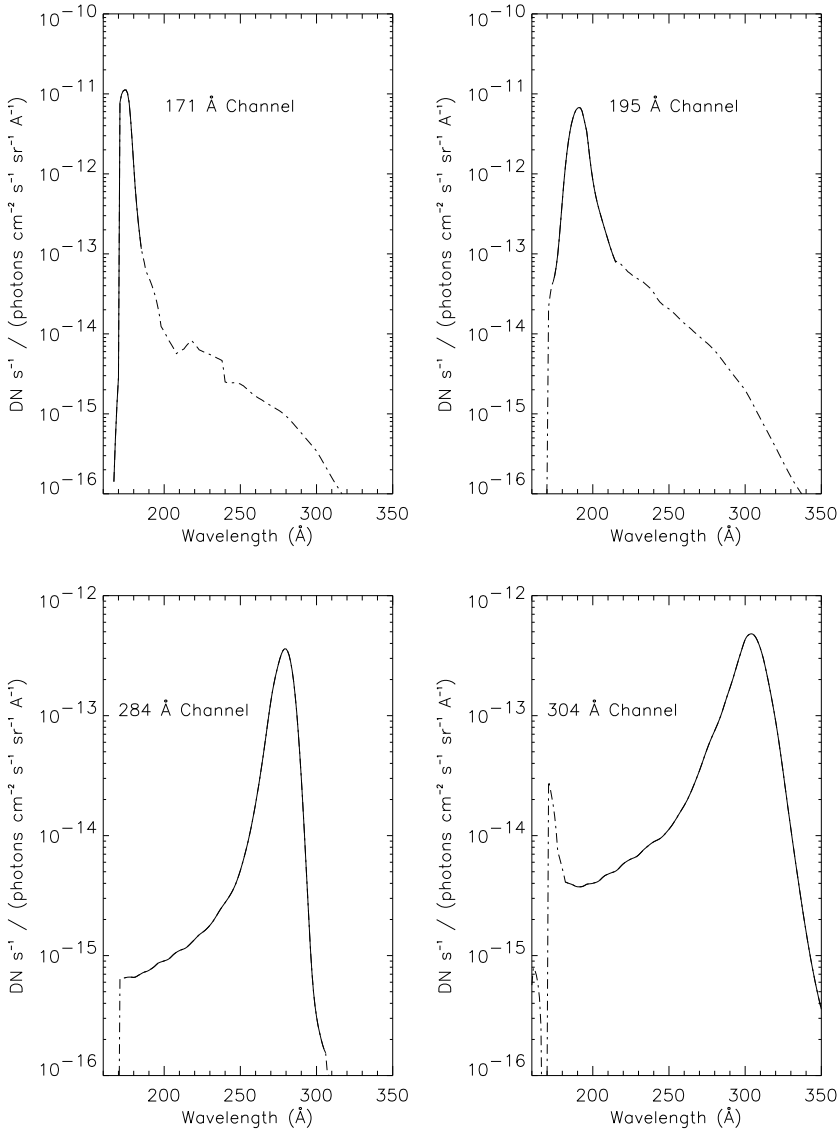

Figure 8.3: Instrument efficiencies for the four EIT bandpasses.

ure 8.4). The extracted patterns were normalized to unity and multiplied by the geometrical obstruction factor of the grid mesh. Those grid corrections are now part of the `eit_prep` tool, but too few images were made in the Al+2, Block-East and Block-West filter wheel positions to allow the extraction of a good correction-pattern for those filters. The amplitude of the grid modulation is large, amounting to 20 % peak-to-peak (5 % rms) in the

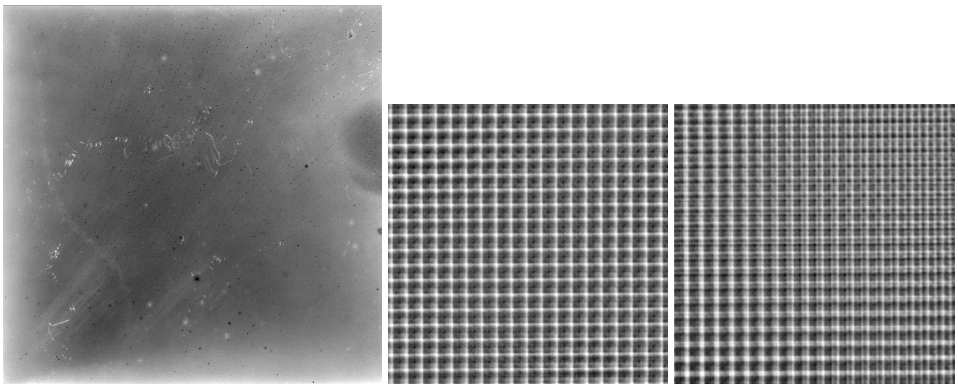

Figure 8.4: Pre-flight CCD flat-field (left) and the extracted grid pattern in the Clear (center) and Al+1 (right) filter-wheel positions, i.e., with the fixed focal Al filter alone or superimposed with the redundant Al filter on the filter wheel (only middle portions of the grids spanning 1/4 of the field-of-view are shown).

Clear position and 17 % peak-to-peak (3 % rms) in the Al+1 position. Furthermore, all grid patterns are modulating the radiation-induced ageing effects which are described below.

8.3.2 EIT Optical Properties

The core part of the EIT optical point-spread function (PSF) was determined by interferometry (wavelength: 633 nm) and wave-front error analysis [*Defise*, 1999]. In flight, the exact focus setting of the instrument has been established by using the sub-pixel decentering of the optical PSF associated with the asymmetrical entrance pupil of each mirror sector. The default thermal-focus setting, which has been maintained throughout the mission, has in fact a 253 μm defocus (0.33 pix decenter): the optical PSF core is 10 μm wider, causing a 50 % increase of the effective PSF width [*Defise et al.*, 1999].

Finally, using simultaneous EIT and MDI images taken during the SOHO offpoint of 3 to 4 April 1996, the plate scale was measured to be $(2.629 \pm 0.001)''$ per pixel [*Auchère et al.*, 2000].

8.3.3 In-flight PSF Wings and Straylight

The straylight and far-wings of the PSF were determined by combining different and independent pieces of evidence: occasional flare images (only in the 19.5 nm quadrant), relative off-limb straylight profiles from a SOHO controlled roll sequence (date: 20 March 1997; 12 positions; 30° steps, KLL extraction algorithm) and the absolute calibration provided over a few locations during the Mercury transit of 15 to 16 November 1999. The various data showed a good consistency and allowed us to derive an extended PSF profile (Figure 8.5), which is elongated along one diagonal and reaches a peak response of 60 %. This means that 40 % of the light at any position is diffused into the far wings. As the brightest sources are on the solar disk, the resulting straylight background is large off the

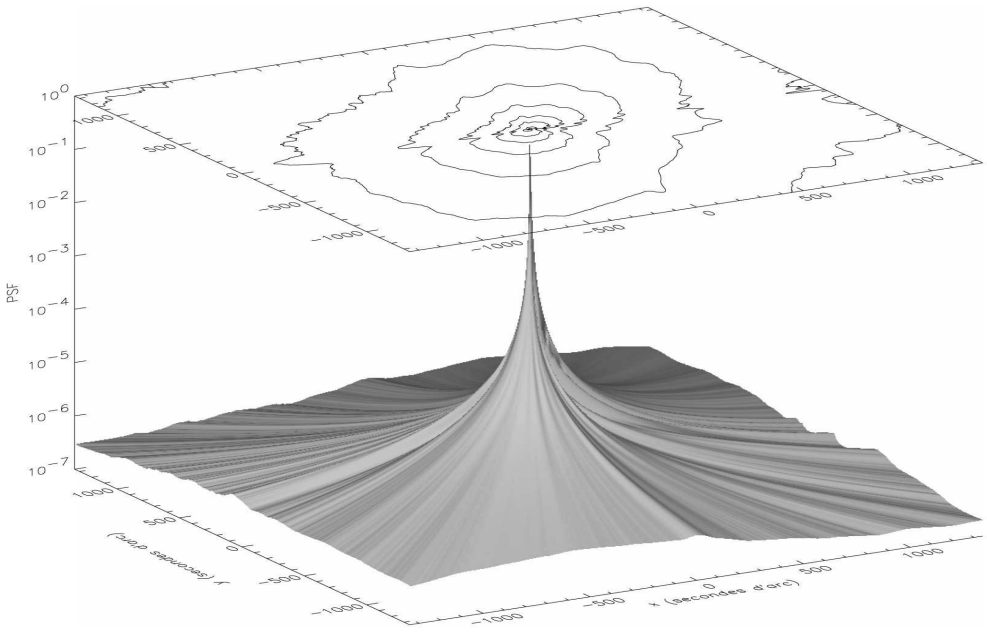

Figure 8.5: PSF extended wings as determined from flare images over a 2630″ square area (equivalent to the full EIT field-of-view), showing the asymmetry along a diagonal which can be attributed to the asymmetric pupil and baffling for each mirror quadrant.

limb: in 30.4 nm images, it reaches 40 % of the average local intensity at 1.2 $R_\odot$, 70 % at 1.4 $R_\odot$ and 80 % at 1.6 $R_\odot$(corners of the field-of-view) [*Auchère*, 2000; *Auchère et al.*, 2001]. As no straylight correction has been implemented in the software yet, radiometric measurements can thus be strongly biased in off-limb regions far from the limb.

8.3.4 Other Factors Affecting the Radiometric Calibration

For completeness, let us also mention the presence of light leaks due to tiny pinholes in the Al filters, which allow some visible light to reach the focal plane. One leak was present right after launch in 28.4 nm images at the North edge of the field-of-view (Clear filter position). In February 1998, new pinholes formed and severely affected all four bandpasses. Since then, all images have been taken with the Al+1 redundant filter, which has no detectable visible-light leak. The optical vignetting of the telescope was modelled by ray tracing and consists only of a small, smooth correction reaching a maximum of 6 % in one corner of the field-of-view [*Defise et al.*, 1999].

Finally, we found recently (2001) that the CCD sensor had a photometric offset between images taken at full resolution and those taken in the two-by-two binned mode (the difference is 5 DN[1]).

[1]DN = Digital Number; raw units of the analogue-to-digital converter in the CCD camera. 1 DN corresponds to 17 electrons in the case of EIT, which has a 14-bit converter, providing a 14 000 DN dynamic range.

This offset and a small, long-term drift of the offset are now corrected in the `eit_prep` routine.

8.4 In-flight Calibration of the Response Degradation

Early in the SOHO mission, it was recognized that the instrument response is undergoing a time-varying degradation. This radiation-induced loss of instrument efficiency has now become the largest correction factor in the EIT calibration. Details concerning the degradation and initial investigations have been discussed by *Moses et al.* [1997], *Defise et al.* [1997, 1998] and *Defise* [1999]. These papers have discussed the case for two sources of degradation, a condensate on the CCD and an EUV-induced spatially-localized decrease in charge collection efficiency (CCE). Complete details of the in-flight calibration of EIT are given in *Newmark et al.* [2002].

8.4.1 Degradation

The degradation process consists of several components which are difficult to separate. The two basic processes contributing to the degradation are the absorption by a surface contaminant of the EUV light, before it interacts with the CCD, and the reduction of CCE in the CCD due to EUV-induced device damage. The first component was significant during the first 2.5 years of the mission, until February to April 1998. During this latter period, most of the contaminant was apparently driven off (possibly related to the increase in pinholes in the front filter). Subsequently, the loss of spacecraft attitude control during the mission interruption (June to October 1998) resulted in significant heating ($> 30\,^{\circ}\mathrm{C}$) for the EIT CCD and annealed part of the electronic damage. The second component has continued to be significant throughout the mission. As the average EUV intensity in the coronal and transition-region images is highly non-uniform, the resulting burned-in flat-field pattern contains strong residuals of local solar-activity features.

The condensation of contaminant on the CCD is expected, since the detector is one of the coldest surfaces in the instrument. In anticipation of in-flight contamination, a cleanliness program was maintained in the construction of the instrument and heaters for the CCD were included in the design. Accumulation of contamination at a constant rate will result in an exponential decline in response. If no polymerization of an organic component is involved, then the condensate will evaporate rapidly during temperature cycling. The straylight baffling around the CCD unfortunately reduces the vacuum conductance out of the vicinity of the CCD, so that further outgassing during a temperature cycle is not feasible.

One can distinguish between the effect of an absorbing surface contaminant and the loss of CCE in the device. Since each interacting EUV photon generates more than one electron, the CCE can be determined by the comparison of the observed signal to the photon shot noise. However, the practical limitations of the CCE analysis from signal-to-noise measurements are significant. Since there is no EUV flat-field illumination capability on EIT, the signal-to-noise ratio must be determined from the solar illumination. The application of this technique to determine the portion of the cumulative degradation from ordinary operations which can be attributed to CCE degradation is discussed in *Defise et al.* [1997], based upon analysis of the Naval Research Laboratory (NRL) EIT Calibration Rocket

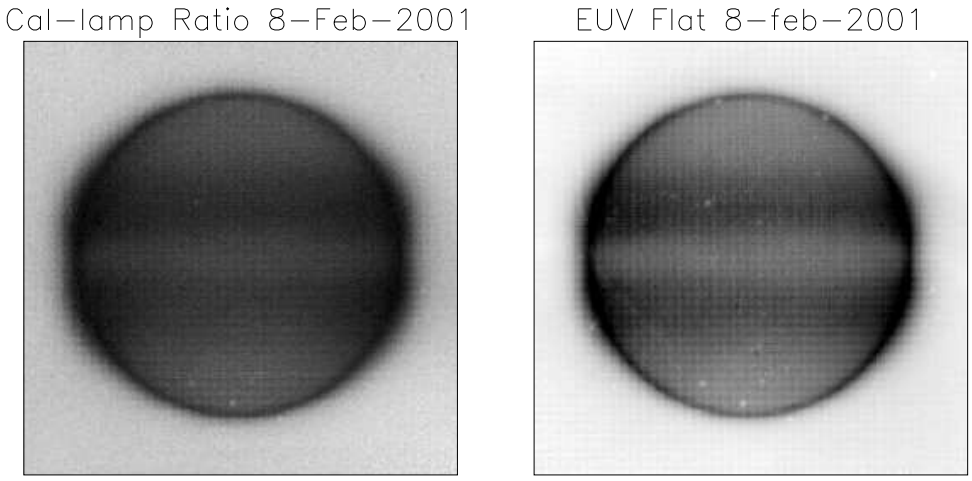

Figure 8.6: EUV flat-field derived from the SOHO offpoint manœuvre of 8 February 2001 (right) and the corresponding calibration lamp ratio (left).

(CalRoc) flown on 16 October 1997. However, the CCE analysis allowed us, for instance, to demonstrate that the degradation of the device for the 29 July 1996 shutter-hang event was totally due to CCE degradation.

8.4.2 Flat-fields

Additional information concerning the CCE decrease can be obtained by examining the visible-light calibration lamp (cal-lamp) images. Most thin condensate layers are transparent to visible photons, so these images should provide information only on the pattern of CCE loss. Indeed, although cal-lamp images do not give direct information in the EUV wavelength range, it was recognized by *Clette* [1998] using NRL CalRoc data that a monotonic relationship exists between the observed CCE loss, as determined above, and the loss of response observed in the cal-lamp images. This work has now been extended using EUV flat-fields derived from a series of offpoints of the SOHO spacecraft, using the KLL method.

Figure 8.6 (right) represents the EUV flat-field determined by *Auchère* [2000] using offpoints generated by spacecraft manœuvres on 8 February 2001. It is compared with an equivalent visible-light flat-field (left) obtained by taking the ratio of a cal-lamp image for that day with the first cal-lamp image taken before any EUV dose accumulated on the detector. Solar features are clearly visible in the flat-field in the form of a negative imprint of an average solar disk, plus limb brightening and plus active-region belts. However, as the Kuhn algorithm only gives relative gain variations, the absolute scale factor must be fixed separately. As the corners of the CCD (1.5 $R_{\odot}$) receive very little EUV radiation, we have assumed that the CCE loss is negligible here and we have thus rescaled the whole map to adjust the corners to unit gain.

Figure 8.7 is a scatter plot showing the relationship between the cal-lamp ratio (Cal-lamp at time t / Initial cal-lamp) and the EUV flat-field for two different days. Clearly,

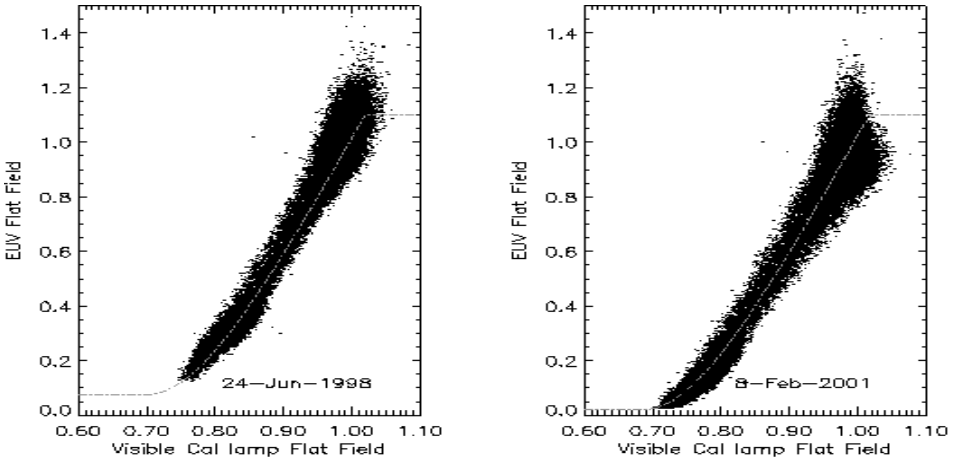

Figure 8.7: Visible to EUV relationship for the June 1998 accidental SOHO attitude loss (left) and for the February 2001 SOHO controlled offpoint (right). Dashed lines show the fitted conversion curves used in the ageing-correction software.

there is a tight relationship and also some time-variability which depends upon the depth of the degradation. We use these data, plus those from two other days, to define our functional relationship between EUV and visible, which is dependent upon the level of visible degradation (dashed lines overplotted on each day). We have taken cal-lamps regularly throughout most of the mission. Therefore, given the above relationship, we can construct, by interpolation, a daily EUV flat-field correction for each pixel.

8.4.3 Corrected Images

The above correction accounts for the CCE effects which dominate the degradation. One way to look at the magnitude and accuracy of the correction is to examine the summed flux (irradiance) of the corrected daily images for each bandpass. The magnitude of the irradiance correction is a factor of ten by early 2001. We find that this correction is within ± 30 % of the total correction. The contaminant portion of the degradation has not yet been accounted for and there are systematic local deviations in the flat-fields due to a number of factors. These include lack of good time-coverage of cal-lamps early in the mission, difficulty in understanding the time period between February and April 1998, and any long-term trends due to slight changes in the filter transmittances or mirror reflectances.

In order to correct for the contaminant and minimize the other systematic errors, we perform a correlation between the CCE-corrected EIT irradiance and a solar index. In this procedure, we assume that this correction is uniform over the CCD. We need to find the coefficients K_1, K_2, K_3, K_4 that optimize the relation: $F/(K_1 \times e^{(K_2 \times time)}) = (K_3 + K_4 \times Index)$, where F is the CCE-corrected irradiance and $Index$ is our chosen solar-activity index. The left side of this equation is then our final corrected irradiance and therefore, the corrected pixel-by-pixel flux. This correlation is performed for each time period between CCD bakeouts. We have investigated the use of various solar indices (for example the SOHO Solar EUV Monitor (SEM, 26.0 nm to 34.0 nm, *Judge et al.* [1998]),

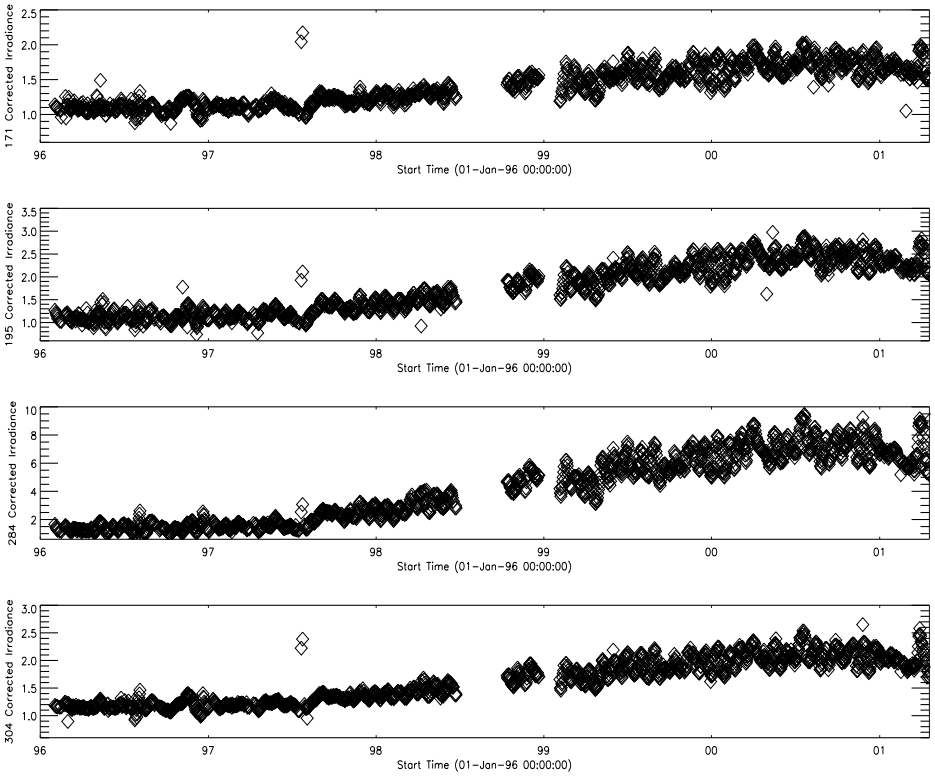

Figure 8.8: Corrected EIT irradiances over the whole mission (normalized to 1 February 1996) in the four EIT bandpasses.

the F10.7 cm radio flux, and the SUSIM Mg II index), and we find almost identical results with each choice. We use the SUSIM Mg II index in our final correlation. This choice and comparisons to other indices are discussed in detail in *Newmark et al.* [2002].

It is important to stress that, in performing this correlation, we are not insisting the EIT data match the chosen solar index, only that there is a linear relationship between the two. The magnitude of this correction is ± 20 % in any time period.

The final relative irradiance over the entire SOHO mission is shown in Figure 8.8. The corrected irradiance shown here has been normalized to 1 February 1996 (shortly after EIT first-light and initial outgassing). This correction can be obtained through the `eit_prep` software tool in the SSW package.

8.5 Conclusions

Table 8.2 provides an overview of all calibration components of EIT, distinguishing the constant and time-dependent corrections and indicating those which are implemented in the SSW EIT routines. EIT being an imager, radiometric calibration and flat-field extrac-

Table 8.2: Constant versus time-varying corrections. "**[SSW]**" indicates the corrections which are embedded in the software. *Italics* highlight the corrections still requiring further analysis.

Constant components	**Variable components**
– Bandpasses, plasma response **[SSW]**	*– Radiometric calibration (ageing), line ratio (absolute)*
– CCD flat-field (initial, local) **[SSW]**	– CCD radiation-induced aging **[SSW]**
– Grid corrections **[SSW]**	*– Light leaks (focal filter pinholes)*
– Straylight (PSF far wings)	– PSF core and focus
– Optical vignetting	– CCD offset value **[SSW]**

tion are intimately related, although those corrections were generally obtained separately and by independent methods. Thanks to its wide field-of-view, EIT can play a special role by providing a connection between absolute global indices (whole-Sun irradiance monitors) and local absolute intercalibrations (subfields, spectrometers). Now that a good integrated calibration has been achieved, EIT can act as a pivot point in the global context of the SOHO intercalibration: a role that was not considered earlier in the mission.

Regarding the future, the continuous monitoring of various classes of solar features, like active-region, bright-point or network brightness distributions, has now been undertaken and could provide standard candles against which long-term instrumental trends could then be validated and better interpreted. For future intercalibration runs, our past experience has shown the extreme importance of two requirements to make intercomparisons more accurate or in some cases even simply valid. These are a knowledge of the spectral irradiance across the broad EIT passbands (spectral scans, DEM modelling) and the accurate timing and close simultaneity (solar variability effects) of observations.

Finally, given the difficulties that we faced when calibrating EIT, we would make the following suggestions in the perspective of future EUV imagers. On-board, multiple LED sources (blue-green LED) or an internal EUV diffusor would greatly help in the interpretation and correction of instrument ageing. The calibration would also be simplified and improved by the introduction of new visible-blind radiation-hard sensors (no cooling, single visible-blocking filter). Even with the present technology, we have learned that significant improvements could be obtained by a more accurate exposure control (shutter mechanism, electronic shuttering), by the mandatory completion of a pre-flight end-to-end calibration of the integrated experiment, by a pre-flight bakeout strategy evaluation (higher temperature, duration) and also by laboratory characterizations of ageing properties (multilayer coatings, sensor CCE).

Acknowledgements

The authors would like to thank K. Wilhelm and E. Verwichte for their useful comments and corrections. Authors JSN and JDM received support from NRL, the Office of Naval Research and NASA grant NDPRS-92385.

Bibliography

Auchère, F., DeForest, C.E., and Artzner, G., In-flight determination of the plate scale of the Extreme-ultraviolet Imaging Telescope, *Astrophys. J.* **529**, L115–L117, 2000.

Auchère, F., *Contribution à l'étude de l'hélium dans la couronne solaire: Observations du télescope EIT*, PhD Thesis, Univ. Paris 6, IAS, Orsay, 2000.

Auchère, F., Hassler, D.M., Slater, D.C., and Woods, T.N., SWRI/LASP Sounding rocket inter-calibration with the EIT instrument on board SOHO, *Sol. Phys.* **202**, 269–280, 2001.

Clette, F., *LASCO/EIT Consortium meeting*, Coolfont WV, 1998.

Defise, J.-M., Clette, F., Moses, J.D., and Hochedez, J.-F., In-orbit diagnostics of EIT EUV CCD radiation-induced ageing, *Proc. SPIE* **3114**, 598–607, 1997.

Defise, J.-M., Moses, J.D., and Clette, F., In-orbit performances of the EIT instrument on board SOHO and intercalibration with the EIT Calroc Sounding Rocket program, *Proc. SPIE* **3442**, 126–139, 1998.

Defise, J.-M., Clette, F., and Auchère, F., In-flight characterization and compensation of the optical properties of the EIT instrument, *Proc. SPIE* **3765**, 341–350, 1999.

Defise, J.-M., *Analyse des performances instrumentales du télescope spatial EIT*, PhD Thesis, Univ. de Liège, 1999.

Delaboudinière, J.-P., Artzner, G.E., Brunaud, J., Gabriel, A.H., Hochedez, J.F., Millier, F., Song, X.Y., Au, B., Dere, K.P., Howard, R.A., Kreplin, R., Michels, D.J., Moses, J.D., Defise, J.M., Jamar, C., Rochus, P., Chauvineau, J.P., Marioge, J.P., Catura, R.C., Lemen, J.R., Shing, L., Stern, R.A., Gurman, J.B., Neupert, W.M., Maucherat, A., Clette, F., Cugnon, P., and van Dessel, E.L., EIT: Extreme-Ultraviolet Imaging Telescope for the SOHO Mission, *Sol. Phys.* **162**, 291–312, 1995.

Dere, K.P., Moses, J.D., Delaboudinière, J.-P., Brunaud, J., Carabetian, C., Hochedez, J.-F., Song, X.Y., Catura, R.C., Clette, F., and Defise, J.-M., The preflight photometric calibration of the Extreme-ultraviolet Imaging Telescope EIT, *Sol. Phys.* **195**, 13–44, 2000.

Dhez, P., Jourdain, E., Hainaut, O., Hochedez, J.-F., Labeque, A., Salvetat, P., and Song, X.Y., Institut d'Astrophysique Spatiale (IAS) 0.1- to 15-keV synchrotron radiation facility beam lines, *Proc. SPIE* **3114**, 134–142, 1997.

Judge, D.L., McMullin, D.R., Ogawa, H.S., Hovestadt, D., Klecker, B., Hilchenbach, M., Möbius, E., Canfield, L.R., Vest, R.E., Watts, R., Tarrio, C., Kühne, M., and Wurz, P., First solar EUV irradiances obtained from SOHO by the CELIAS/SEM, *Sol. Phys.* **177**, 161–173, 1998.

Kuhn, J.R., Lin, H., and Loranz, D., Gain calibrating nonuniform image-array data using only the image data, *Publ. Astron. Soc. Pac.* **103**, 1097–1108, 1991.

Moses, D., Clette, F., Delaboudiniere, J.-P., Artzner, G.E., Bougnet, M., Brunaud, J., Carabetian, C., Gabriel, A.H., Hochedez, J.F., Millier, F., Song, X.Y., Au, B., Dere, K.P., Howard, R.A., Kreplin, R., Michels, D.J., Defise, J.M., Jamar, C., Rochus, P., Chauvineau, J.P., Marioge, J.P., Catura, R.C., Lemen, J.R., Shing, L., Stern, R.A., Gurman, J.B., Neupert, W.M., Newmark, J., Thompson, B., Maucherat, A., Portier-Fozzani, F., Berghmans, D., Cugnon, P., van Dessel, E.L., and Gabryl, J.R., EIT observations of the extreme ultraviolet Sun, *Sol. Phys.* **175**, 571–599, 1997.

Newmark, J.S., Moses, J.D., Cook, J.W., Delaboudinière, J.-P., Song, X.Y., Carabetian, C., Bougnet, M., Brunaud, J., Defise, J.-M., Clette, F., and Hochedez, J.-F., Calibration and

flight of the NRL EIT CalRoc, *Proc. SPIE* **4139**, 328–339, 2000.

Newmark, J.S., SOHO - EIT User's Guide, Chapter 6: EIT Calibration, `http://umbra.nascom.nasa.gov/eit/eit_guide/guide.html`, 2000.

Newmark, J.S., Cook, J.W., Auchère, F., Moses, J.D., and Clette, F., In-Flight Calibration of SOHO EIT, in preparation, 2002.

Song, X.Y., Caractérisation et étalonnage radiométrique du télescope solaire EIT à l'aide du rayonnement synchrotron (entre 10 et 100 nm), PhD Thesis, Univ. Paris-Sud, IAS, Orsay, 1995.